Supporting Information for "Disintegration and Buttressing Effect of the Landfast Sea Ice in the Larsen B Embayment, Antarctic Peninsula"

Yudong Sun[1], Bryan Riel[1,2]and Brent Minchew[1]

[1]Department of Earth, Atmospheric, and Planetary Sciences, Massachusetts Institute of Technology, Cambridge, MA, USA

[2]School of Earth Sciences, Zhejiang University, Hangzhou, Zhejiang, China

Contents of this file

1. Text S1

2. Figures S1 to S2

Additional Supporting Information (Files uploaded separately)

1. Captions for Movies S1 to S5

Introduction

The Supplementary Material consists of the following parts:

Supplementary text S1 describes data and methods for pixel offset tracking, filtering,

measuring fast ice extent, and calculating strain rate.

Figure S1 compares velocity data before and after tide correction and median filtering.

Figure S2 shows time-series inversion for velocity curve fitting and its "L-curve".

Movie S1 is a SAR movie.

Movie S2 and S3 are horizontal velocity maps with different filtering.

———————

April 10, 2023, 12:47am

Movie S4 and S5 are the strain rate maps.

High-resolution movies can be found at:

`https://drive.google.com/drive/folders/1OSnWMyDJBEQifgNMruqSgHdfDu8QQbzb?usp=share_link`

Text S1. Data and methods

1. SAR pixel offset tracking

SAR data We use C-band Copernicus Sentinel-1 synthetic aperture radar (SAR) data from 2014 to 2022, retrieved from ASF DAAC and processed by ESA. We use the software "hyp3_timeseries" (`https://github.com/jlinick/hyp3_timeseries`) to make a time-lapse SAR movie (Supplementary Movie S1). Sentinel-1A and Sentinel-1B have a 12-day revisit period, so the shortest interval is 6 days if our area is visited by one satellite and followed by the other. We use the interferometric wide swath Single-Look-Complex (SLC) products on a descending track (path 38) with a platform heading direction of about 23° to the west of south. The incidence angles for three swaths are 32.9°, 38.3°, and 43.1°, and the pixel size is 2.3×14.1 m in the range and azimuth directions.

Pixel offset tracking We calculate near-instantaneous velocity on the glacier surface from the relative displacement during the revisit interval, 6 and 12 days. The displacement of a specific ground target can be measured by comparing the offset between the pixel locations of that target from two co-registered SAR images. The pixel offset tracking technique involves applying a two-dimensional cross-correlation operation between multiple image patches of finite size between the reference and secondary images. Each cross-correlation operation results in a correlation surface, and the location of the peak of that surface is proportional to the displacement between the image patches. We slide a patch with a finite size (256×64 pixels) to do the cross-correlation with a search window

size as 40×10 pixels. In this way, we create a dense offset map with a skip width and height between patches as 128 and 32 pixels. Therefore, the maximum velocity we can measure is about 7.7 m/day if the time interval is 12 days. The precision of pixel offset tracking is about one-tenth of the pixel size, so the speed error is about 0.24 m/day for a 6-day interval (Strozzi et al., 2002). We use the InSAR Scientific Computing Environment ISCE (Rosen et al., 2012) to perform the pixel offset tracking. In order to do the stack processing, which produces a stack of precisely co-registered SAR images, we use the "topsStack" package implemented in the ISCE environment (Fattahi et al., 2016). The topography model used for co-registration and removal of processing artifacts is the Reference Elevation Model of Antarctica REMA (Howat et al., 2019).

Tide correction We use the tide model CATS2008 (Padman et al., 2002, 2008), to infer the displacements in the horizontal plane. Because we are measuring three-dimensional motion with only two-components of observations (slant-range and azimuth), we cannot uniquely recover the horizontal motion. Therefore, we utilize the CATS2008 tide model to reduce our degrees of freedom by one. The horizontal range displacement d_{rh} is given by

$$d_{rh} = \frac{d_r + z \cos \theta}{\sin \theta}, \tag{1}$$

where d_r, z, and θ are range displacement, vertical tide displacement, and incidence angle of the satellite, respectively. d_{rh} (blue dots) is compared with $d_r / \sin \theta$ (red dots) and the former has a lower deviation in Figure S1.

Filtering We process the displacement fields with a median filter because they are noisy where the coherence is low. Coherence is the magnitude of complex correlation between two SAR images. For example, the coherence for the landfast sea ice is low in summer

April 10, 2023, 12:47am

when the surface ice melts and changes the scattering geometry (Strozzi et al., 1999). First, we smooth data in the space and time domain by the median filter (blue line in Figure S1) with window sizes about 0.7×0.7 km and 12 days, which reduces the noise and does not smear the fine structures of shear zones. Second, we mask the data with high spatial and temporal gradients to remove the noisy areas such as oceans and areas with surface melting.

2.   Fast ice extent

We measure the landfast sea ice extent to study its evolution and relationship with upstream glaciers. The landfast ice is suggested to be defined as the ice pack attached to the coast and remaining still for 20 days (Mahoney et al., 2006). SAR is often used to study the landfast ice because SAR comes from active microwave sensors that can image in day or night conditions and whose long (microwave) wavelengths effectively penetrate cloud cover. Mahoney, Eicken, Graves, Shapiro, and Cotter (2004) identify landfast ice by calculating the difference in spatial gradients between SAR images, while Giles, Massom, and Lytle (2008) use cross-correlation methods to find the stationary fast ice that has a low offset. We choose the second method to delineate the seaward landfast ice edge (SLIE) and use the coastline (Mouginot et al., 2017) and SLIE to estimate the area of the landfast ice. Specifically, we identify the landfast ice that moves less than 100 m within 12 days.

3.   Time-series inversion

We fit the time-series velocity curve of a given location on ice shelves or landfast sea ice (Movie S3) to study the temporal change and its controlling factors. The time-series

April 10, 2023, 12:47am

signal is decomposed into secular, seasonal, and transient terms. We use the time series inversion package "iceutils.tseries" (Riel et al., 2014, 2021) to do the regression problem as $Gm = d$, where matrix G consists of the temporal basis functions we use to construct the time-series signal, and m and d are the model and data vectors. We get the unique solution to minimize the cost function ϕ as $\phi = ||Gm - d||_2^2 + \lambda ||m||_{1,2}$, using L1-norm or L2-norm regularization with a penalty parameter λ.

The dictionary G includes a linear function, sinusoidal functions with periods of 0.5 and 1 year, and integrated B-splines, which are smooth step functions, with different time scales from 10 to 640 days (Hetland et al., 2012). We repeat the inversion with different penalty parameters λ and construct the L-curve, which illustrates the data misfit versus the norm of the coefficient vector, to choose the "best" λ and determine the degree of overfitting (e.g. Figure S2). We select the value for λ roughly at the corner of the L-curve, 0.1 for L2-norm (ridge regression), and 0.03 for L1-norm regularization (lasso regression).

4. Strain rate map

Strain rate maps are helpful to illustrate the shear bands and rifts, and evaluate the stress state of the ice. We derive the horizontal strain rate tensor $\dot{\boldsymbol{\epsilon}}$ from the velocity field as follows

$$\dot{\boldsymbol{\epsilon}} = \begin{pmatrix} \dot{\epsilon}_{xx} & \dot{\epsilon}_{xy} \\ \dot{\epsilon}_{yx} & \dot{\epsilon}_{yy} \end{pmatrix} = \begin{pmatrix} \frac{\partial U}{\partial x} & \frac{1}{2}\left(\frac{\partial U}{\partial y} + \frac{\partial V}{\partial x}\right) \\ \frac{1}{2}\left(\frac{\partial U}{\partial y} + \frac{\partial V}{\partial x}\right) & \frac{\partial V}{\partial y} \end{pmatrix}, \tag{2}$$

where U and V are horizontal velocity in x and y directions. The dilation strain rate $\dot{\epsilon}_{dilate}$ in the horizontal plane is

$$\dot{\epsilon}_{dilate} = \dot{\epsilon}_{xx} + \dot{\epsilon}_{yy}, \tag{3}$$

where we adopt the convention that $\dot{\epsilon}_{dilate}$ is positive in tension. If we assume that ice is incompressible ($\dot{\epsilon}_{xx} + \dot{\epsilon}_{yy} + \dot{\epsilon}_{zz} = 0$), we have $\dot{\epsilon}_{zz} = -\dot{\epsilon}_{dilate}$, indicating that the value of the dilatant strain rate is independent of our choices for the horizontal coordinates x and y. In other words, the incompressibility of ice directly uniquely relates to the dilatant strain rate to the first invariant (*i.e.* trace) of the 3D strain rate tensor. The maximum shear strain rate $\dot{\epsilon}_{shear}$ is similarly invariant to the horizontal coordinate system and is defined as

$$\dot{\epsilon}_{shear} = \sqrt{\frac{1}{4}(\dot{\epsilon}_{xx} + \dot{\epsilon}_{yy})^2 + \dot{\epsilon}_{yx}^2 - \dot{\epsilon}_{xx}\dot{\epsilon}_{yy}}, \tag{4}$$

as suggested by Nye (1959) and Harper, Humphrey, and Pfeffer (1998). This formulation is equivalent to one-half the difference in the maximum and minimum principal strain rates. The effective strain rate $\dot{\epsilon}_E$, which is often used in Glen's law, is the square root of the second invariant of the strain rate tensor (Cuffey & Paterson, 2010), defined as

$$\dot{\epsilon}_E = \sqrt{\dot{\epsilon}_{xx}^2 + \dot{\epsilon}_{yy}^2 + \dot{\epsilon}_{xy}^2 + \dot{\epsilon}_{xx}\dot{\epsilon}_{yy}}, \tag{5}$$

where incompressibility and $\dot{\epsilon}_{xz} = \dot{\epsilon}_{yz} = 0$ (due to negligible tangential tractions at the upper and lower surfaces of the ice shelf) are assumed.

To calculate the strain rate, we first rotate the horizontal velocity vector to the south and east coordinates. Then, we smooth the data with the second-order Savitzky–Golay filter (Savitzky & Golay, 1964) with a square window size of about 4 km (Movie S2). The window size is approximately $10 - 20$ times the local ice thickness to remove small-scale dynamical effects that are generally not resolvable with commonly used ice flow equations (Bindschadler et al., 1996). Finally, we calculate the dilation strain rate $\dot{\epsilon}_{dilate}$, maximum shear strain rate $\dot{\epsilon}_{shear}$, strain rate along the flow direction $\dot{\epsilon}_{xx}$, and effective strain rate $\dot{\epsilon}_E$ (Movie S4 and S5).

References

Bindschadler, R., Vornberger, P., Blankenship, D., Scambos, T., & Jacobel, R. (1996). Surface velocity and mass balance of ice streams d and e, west antarctica. *Journal of Glaciology*, *42*(142), 461–475.

Cuffey, K. M., & Paterson, W. S. B. (2010). *The physics of glaciers*. Academic Press.

Fattahi, H., Agram, P., & Simons, M. (2016). A network-based enhanced spectral diversity approach for tops time-series analysis. *IEEE Transactions on Geoscience and Remote Sensing*, *55*(2), 777–786.

Giles, A. B., Massom, R. A., & Lytle, V. I. (2008). Fast-ice distribution in east antarctica during 1997 and 1999 determined using radarsat data. *Journal of Geophysical Research: Oceans*, *113*(C2).

Harper, J. T., Humphrey, N., & Pfeffer, W. T. (1998). Crevasse patterns and the strain-rate tensor: a high-resolution comparison. *Journal of Glaciology*, *44*(146), 68–76.

Hetland, E., Musé, P., Simons, M., Lin, Y., Agram, P., & DiCaprio, C. (2012). Multiscale insar time series (mints) analysis of surface deformation. *Journal of Geophysical Research: Solid Earth*, *117*(B2).

Howat, I. M., Porter, C., Smith, B. E., Noh, M.-J., & Morin, P. (2019). The reference elevation model of antarctica. *The Cryosphere*, *13*(2), 665–674.

Mahoney, A., Eicken, H., Graves, A., Shapiro, L., & Cotter, P. (2004). Landfast sea ice extent and variability in the alaskan arctic derived from sar imagery. In *Igarss 2004. 2004 ieee international geoscience and remote sensing symposium* (Vol. 3, pp. 2146–2149).

Mahoney, A., Eicken, H., Shapiro, L., & Graves, A. (2006). Defining and locating

the seaward landfast ice edge in northern alaska. In *18th international conference on port and ocean engineering under arctic conditions (poac'05), potsdam, ny* (pp. 991–1001).

Mouginot, J., Scheuchl, B., & Rignot, E. (2017). Measures antarctic boundaries for ipy 2007–2009 from satellite radar, version 2. *National Snow and Ice Data Center*, *10*.

Nye, J. F. (1959). A method of determining the strain-rate tensor at the surface of a glacier. *Journal of Glaciology*, *3*(25), 409–419.

Padman, L., Erofeeva, S. Y., & Fricker, H. A. (2008). Improving antarctic tide models by assimilation of icesat laser altimetry over ice shelves. *Geophysical Research Letters*, *35*(22).

Padman, L., Fricker, H. A., Coleman, R., Howard, S., & Erofeeva, L. (2002). A new tide model for the antarctic ice shelves and seas. *Annals of Glaciology*, *34*, 247–254.

Riel, B., Minchew, B., & Joughin, I. (2021). Observing traveling waves in glaciers with remote sensing: new flexible time series methods and application to sermeq kujalleq (jakobshavn isbræ), greenland. *The Cryosphere*, *15*(1), 407–429.

Riel, B., Simons, M., Agram, P., & Zhan, Z. (2014). Detecting transient signals in geodetic time series using sparse estimation techniques. *Journal of Geophysical Research: Solid Earth*, *119*(6), 5140–5160.

Rosen, P. A., Gurrola, E., Sacco, G. F., & Zebker, H. (2012). The insar scientific computing environment. In *Eusar 2012; 9th european conference on synthetic aperture radar* (pp. 730–733).

Savitzky, A., & Golay, M. J. (1964). Smoothing and differentiation of data by simplified least squares procedures. *Analytical chemistry*, *36*(8), 1627–1639.

Strozzi, T., Luckman, A., Murray, T., Wegmuller, U., & Werner, C. L. (2002). Glacier motion estimation using sar offset-tracking procedures. *IEEE Transactions on Geoscience and Remote Sensing*, *40*(11), 2384–2391.

Strozzi, T., Wegmuller, U., & Matzler, C. (1999). Mapping wet snowcovers with sar interferometry. *International Journal of Remote Sensing*, *20*(12), 2395–2403.

Movie S1.

Time-lapse SAR movie in Larsen B area from Sentinel-1.

Movie S2.

Horizontal velocity in east and south direction after Savitzky–Golay filtered and corresponding SAR image.

Movie S3.

Horizontal velocity maps after time-series filtering.

Movie S4.

Maps of dilation strain rate $\dot{\epsilon}_{dilate}$ and maximum shear strain rate $\dot{\epsilon}_{shear}$.

Movie S5.

Maps of strain rate along the flow direction $\dot{\epsilon}_{xx}$ and effective strain rate $\dot{\epsilon}_E$.
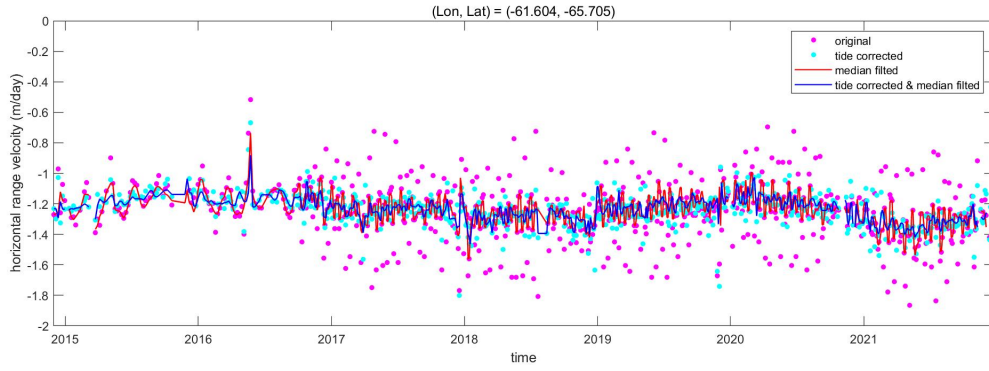
Figure S1. Comparison of horizontal range velocity v_{rh} at one spot on the Scar Inlet Ice Shelf before (red dots) and after tide correction (blue dots). Red and blue lines represent the original and tidal corrected v_{rh} after median filtering.
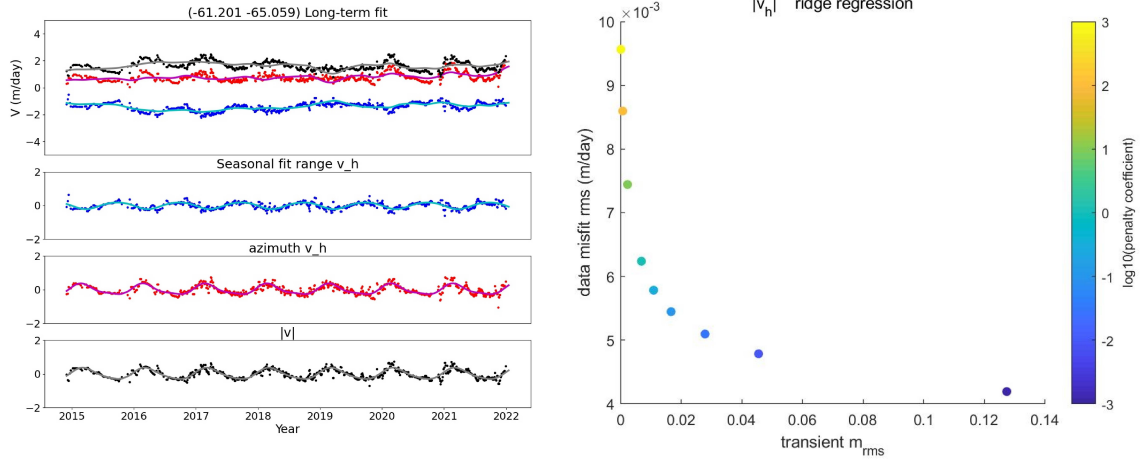
Figure S2. Long-term and seasonal components (a) for a spot on the landfast sea ice and "L curves" for L2-norm regression (b). Solid lines in the upper figures in (a) represent the long-term fitting curves. The seasonal fitting curves (solid lines) and detrended data (dots) are compared in the three lower figures (a). Data misfit and norm of parameter vector are plotted for different penalty coefficients in (b), and the "optimum" coefficient is at the corner of the curve.